

EXPERIMENTAL AND NUMERICAL STUDY OF HYPERVELOCITY IMPACT ON WHIPPLE SHIELDS WITH VARYING BUMPER MATERIALS

Rannveig M. Færgestad⁽¹⁾, Bruce A. Davis⁽²⁾, Christopher J. Cline II⁽³⁾, Eric L. Christiansen⁽³⁾, Kevin A. Ford⁽⁴⁾, Odd S. Hopperstad⁽¹⁾, Jens K. Holmen⁽⁵⁾ and Tore Børvik⁽¹⁾

(1) *Structural Impact Laboratory (SIMLab), Department of Structural Engineering, NTNU – Norwegian University of Science and Technology, Richard Birkelands veg 1a, 7491 Trondheim, Norway, rannveig.m.fargestad@ntnu.no*

(2) *Amentum, NASA Johnson Space Center, Astromaterials Research and Exploration Science, 2101 NASA Parkway Houston, TX 77058, United States*

(3) *NASA Johnson Space Center, Astromaterials Research and Exploration Science, Mail code XI5, 2101 NASA Parkway, Houston, TX 77058, United States*

(4) *Kevin A. Ford Astronautical, LLC*

(5) *Enodo AS, Strømsø torg 4, 3044 Drammen, Norway*

ABSTRACT

Different bumper materials subjected to hypervelocity impact show varying ability to shock and break up an incoming projectile. This paper presents an experimental and numerical study of traditional dual-wall Whipple shields, where four different bumper material configurations are compared to a traditional thin AA6061-T6 bumper, by dimensioning all bumpers to have near equal areal density. The bumpers included in the study are beta cloth (1 layer) in front of a thin AA6061-T6 bumper, Nextel woven fabric (6 layers) and stainless steel mesh (5 layers). All bumpers were impacted by spherical AA2017-T4 projectiles at 7 km/s. Numerical models were then created in LS-DYNA using a coupled finite element-discrete element method (FEM-DEM), showing a close match with the experimental results with similar performance and characteristics.

1 INTRODUCTION

Whipple shields, first introduced in 1947 [1], have been widely used in spacecraft shielding applications, with a wide range of configurations and materials applied for the different layers. The shielding layers, separated by standoff distances, break the projectile into a cloud of material and spreads the energy over a large area. The bumper, the first layer to interact with a projectile, is important in this process, and different materials show different performance when applied as a bumper.

A wide range of materials have been tested and implemented as bumpers [2]. Thin metallic bumpers, typically made up of a single sheet of aluminum, steel or titanium, are the most widely used, with aluminum being the most common of them. Other configurations studied are sandwich panels with either honeycomb or foam cores, woven fabric layers with, e.g., Nextel, Kevlar, Basalt, Beta cloth or UHMWPE, metallic wire mesh materials, various fiber reinforced matrix materials and

ceramic-based materials. To directly compare the performance of the different configurations, systematic studies can be performed where the areal density is kept constant, as presented in [3][4], where six different fabric bumpers were compared with an areal density of around 1.1 g/cm².

Studying the efficiency of bumpers with different materials and near equal areal density is of interest, to determine which materials are better at breaking up incoming projectiles while minimizing the ejecta produced on impact. This paper presents an experimental and numerical study of how the characteristics of the debris cloud and damage on shield layers change for four different bumper materials, and how well numerical models can capture the observed behavior.

2 EXPERIMENTAL DATA

An experimental study of hypervelocity impact on Whipple shields with varying bumper materials is presented in [5], and this paper summarizes a selection of these. All tests were performed at the NASA White Sands Test Facility (WSTF) Remote Hypervelocity Test Facility (RHTL) in Las Cruces, New Mexico using a 0.17-caliber two-stage light-gas gun (LGG).

The Whipple shield configuration for the baseline test with an AA6061-T6 bumper is illustrated in Fig. 1 with dimensions. A standard dual-wall Whipple shield is used, with an added ejecta catcher plate in front of the bumper and a witness plate behind the rear wall. The configuration was kept the same for all tests, except for the bumper, which was replaced with three different bumpers with near equal areal density around 0.17 g/cm². Spherical AA2017-T4 projectiles with a 3.18 mm diameter were used in all tests, and all impacts were at 0° normal to the bumper surface. Ten tests were performed in [5], at 3 and 7 km/s impact velocity, four of the tests at 7 km/s will be studied in this paper.

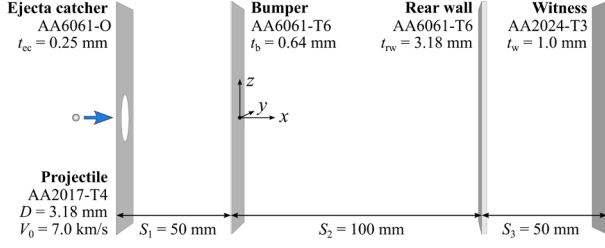


Figure 1: Baseline Whipple shield configuration [5].

The bumper configurations included in this study are presented in Tab. 1, along with an overview of the experimental results. The first configuration is the baseline, a thin sheet of AA6061-T6, the second configuration is one layer of Beta cloth with 36x26 per cm thread count in front of a AA6061-T6 bumper, the third configuration is six layers of Nextel AF-10 woven fabric oriented at $0^\circ/45^\circ/0^\circ/45^\circ/0^\circ/45^\circ$ with a thread count of 18x18 per cm, and the fourth configuration is five layers of stainless steel (SS) 304 wire mesh oriented at $0^\circ/45^\circ/0^\circ/45^\circ/0^\circ/45^\circ$ with a mesh count of 59x59 (i.e., 59 openings per cm) and a wire thickness of 0.066 mm.

The tests were analyzed using high-speed camera footage from a Shimadzu HPV camera at 1 M frames per second, as well as post-test inspections of all plates. Overall, the tests are evaluated on a pass/fail of the rear wall, where perforation or spalling is counted as failure. Further, the configurations are compared by evaluating the damage on the ejecta catcher, bumper, and rear wall. Since none of the tests presented in this paper failed, the witness plate will not be included in the analysis.

Table 1: Overview of experimental data and results [5].

Test #	Bumper material	Number of layers	Areal density, one layer [g/cm ²]	Bumper areal density [g/cm ²]	Bumper thickness, t_b [mm]	Impact velocity, V_0 [km/s]	Residual velocity, V_1 [km/s]	V_1/V_0	Result
1	AA6061-T6 [baseline]	1	0.173	0.173	0.64	6.93	6.37	0.92	Pass
2	Beta cloth + AA6061-T6	2	0.029 + 0.135	0.162	0.2+0.5	6.79	7.11	1.05	Pass
3	Nextel AF-10	6	0.029	0.174	1.8	6.97	7.35	1.05	Pass
4	Wire mesh, SS 304	5	0.033	0.165	1.0	7.10	6.85	0.97	Pass

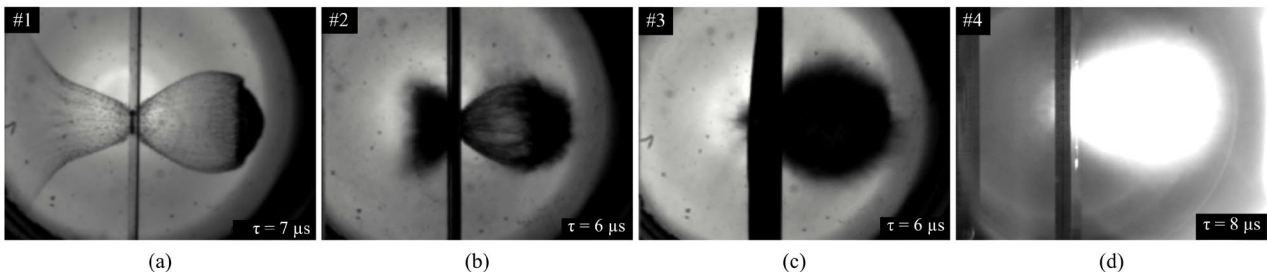


Figure 2: Debris clouds from the experimental campaign [5], for bumper configurations: (a) AA6061-T6, (b) Beta cloth + AA6061-T6, (c) Nextel AF-10, (d) SS 304 wire mesh.

The debris clouds are presented in Fig. 2 at a similar distance from the bumper for all four tests. The baseline AA6061-T6 bumper generates a typical debris cloud for aluminum Whipple shields at this impact velocity, with a concentration of projectile material in the front of the cloud and a clear outer border. A large amount of ejecta is created from the bumper hole. The debris cloud generated by impact with the Beta cloth bumper is similar to the baseline, with a concentration of material near the front, but dust from the beta cloth layer creates a less distinct outer border, and reduces the amount and velocity of ejecta. The Nextel and SS 304 bumpers share similar characteristics, with a rounded shape and a diffuse outer debris cloud border created by small particles of bumper material, making it challenging to pick out individual fragments and take exact measurements.

The velocity of the front edge of the debris cloud is measured in each test, denoted the residual velocity V_1 in this paper, and is presented in Tab. 1. The ratio of V_1 and the impact velocity V_0 is found to be just under one for the baseline and SS wire mesh configurations, i.e., the residual velocity of the debris cloud is lower than the impact velocity of the projectile before impact. For the Nextel and Beta cloth configurations, the residual velocity V_1 is found to be around 5% higher than the impact velocity V_0 . This phenomenon has been observed in other mesh bumper studies (e.g., [6], [7]), and is understood to be due to the jetting effect as the projectile material passes through the openings in the mesh along the rounded wire profiles.

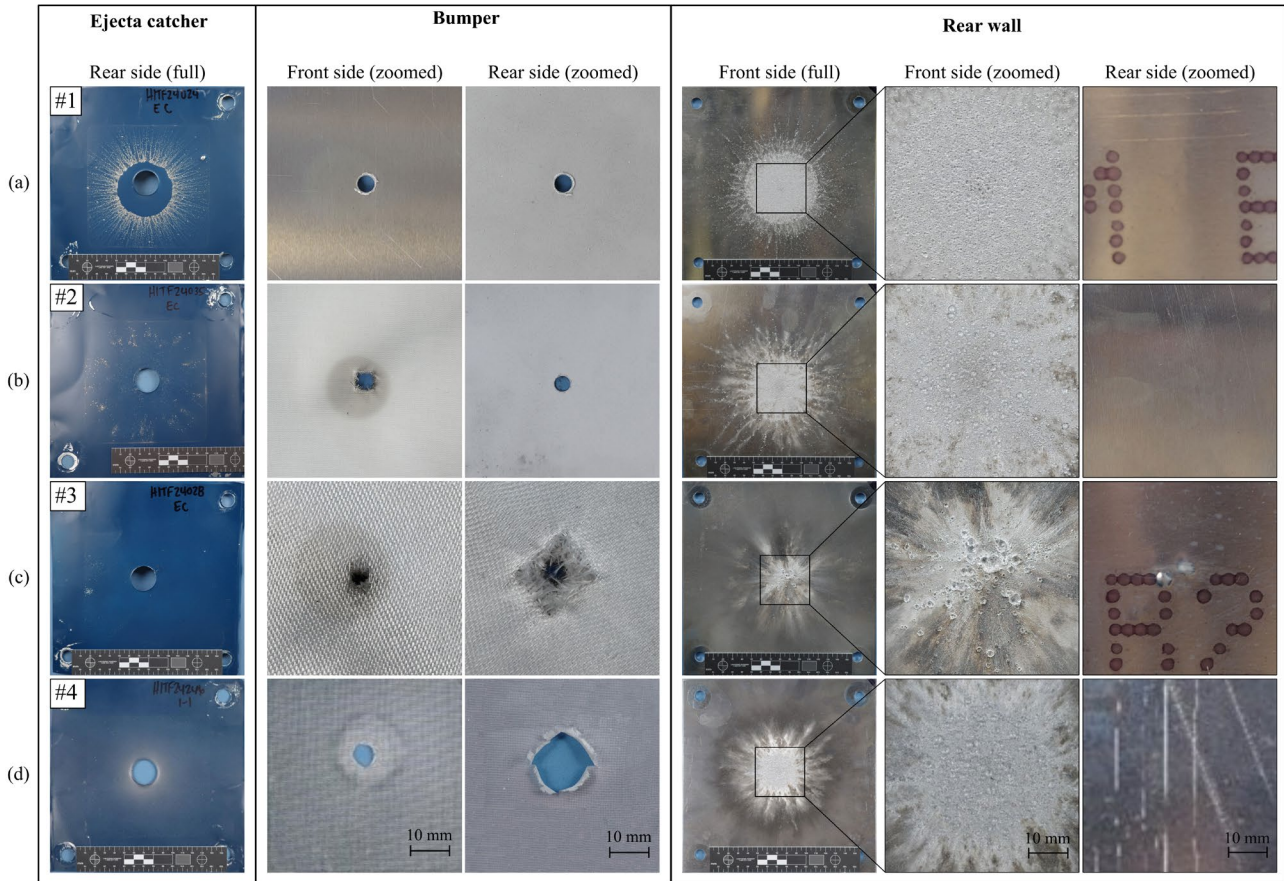


Figure 3: Comparison of damage to shield layers after impact [5]. The ejecta catcher (1st column), bumper (2nd and 3rd column) and rear wall (4th, 5th and 6th column) are presented for configurations with bumper materials: (a) AA6061-T6, (b) Beta cloth with AA6061-T6, (c) Nextel AF-10 and (d) SS 304 wire mesh.

Photographs of each shield layer after impact is presented in Fig. 3. Starting from the front of the shield, the ejecta catchers, positioned in front of the bumpers to capture the ejecta, are presented in the first column. Significantly different ejecta patterns are observed, with the baseline bumper generating the most ejecta, and the Nextel bumper generates hardly any ejecta. The holes in the bumpers are presented in the second and third column, with small and circular holes for the baseline and Beta cloth configurations. For the Nextel and SS 304 bumpers, the hole increases in diameter for each layer in the bumper, and the last layers show unraveling and rips in the woven structure. The craters on the front and rear side of the rear wall are presented in the fourth, fifth and sixth column, with varying levels of crater size, depth and radial distribution. The baseline bumper gives a widely distributed crater pattern with a large circular concentration of small craters in the center. The Beta cloth and SS 304 bumpers show a similar trend, but the craters are larger and located inside a smaller area, resulting in a more concentrated load than for the baseline. However, the Nextel bumper is found to result in the most detrimental damage, with large individual craters at the center of the rear wall, limited radial spread and two bulges on the rear side.

3 NUMERICAL MODELLING

3.1 Model setup and geometry

Numerical models are created for each configuration from the experimental data presented, and simulations are performed in LS-DYNA [8]. In this study, the ejecta catcher and witness plate are omitted from the model, and only a limited section of the bumper and rear wall are modelled to reduce the computational time. The baseline configuration of the numerical model is shown in Fig. 4. The width of the rear wall was set to 90 mm, while the width of the baseline bumper was set to 12 mm.

The geometries of the woven Nextel and Beta cloth bumpers, as well as the SS 304 wire mesh, were created in Solidworks [9] meshed in LS-DYNA, and are presented in Fig. 5. A mesoscale approach is taken in the modelling of the woven fabrics, where the yarns are modelled as homogeneous entities. Eight elements are applied in the cross-section mesh of the Beta cloth yarns, four elements for the Nextel yarns, and two elements for the SS 304 wires. To reduce the computational time, the bumper diameters are cropped to be as small as possible, with an increasing diameter for each layer.



Figure 4: Finite element model of baseline Whipple shield configuration with an AA6061-T6 bumper.

To reduce the computational time further, the rear wall mesh was created with unstructured hexahedral meshing in Gmsh [10], allowing for small elements in the center, coarser elements around the outer edge, and a smooth transition in between. This mesh approach means that craters will be more distinct and detailed in the center and will gradually be less accurate and visible with increasing radial position. The comparison of the rear walls between the experiments and simulations is therefore expected to match more closely in the center of the rear wall.

The modelling approach selected in this study is a coupled finite element-discrete element method [11] in LS-DYNA, which is achieved through the keyword *DEFINE_ADAPTIVE_SOLID_TO_DES. Solid parts are adaptively transformed to particles when the solid elements comprising those parts fail, as illustrated in Fig. 6. The particle replacing the failed element inherits the properties of the element, including mass and kinematical state [12]. Failure of an element can occur either from a failure criterion or from reaching a critical temperature. The method allows for an implicit way of distinguishing larger, solid fragments from molten and/or small fragments in the debris clouds.

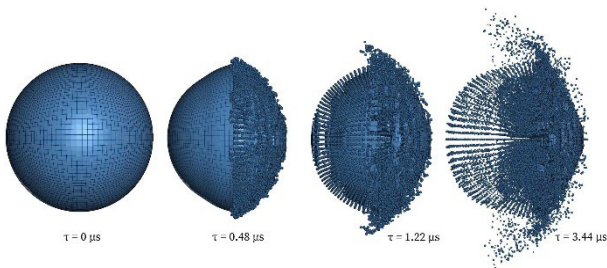


Figure 6: Conversion from finite elements to discrete particles after impact, shown at 6.7 km/s [11].

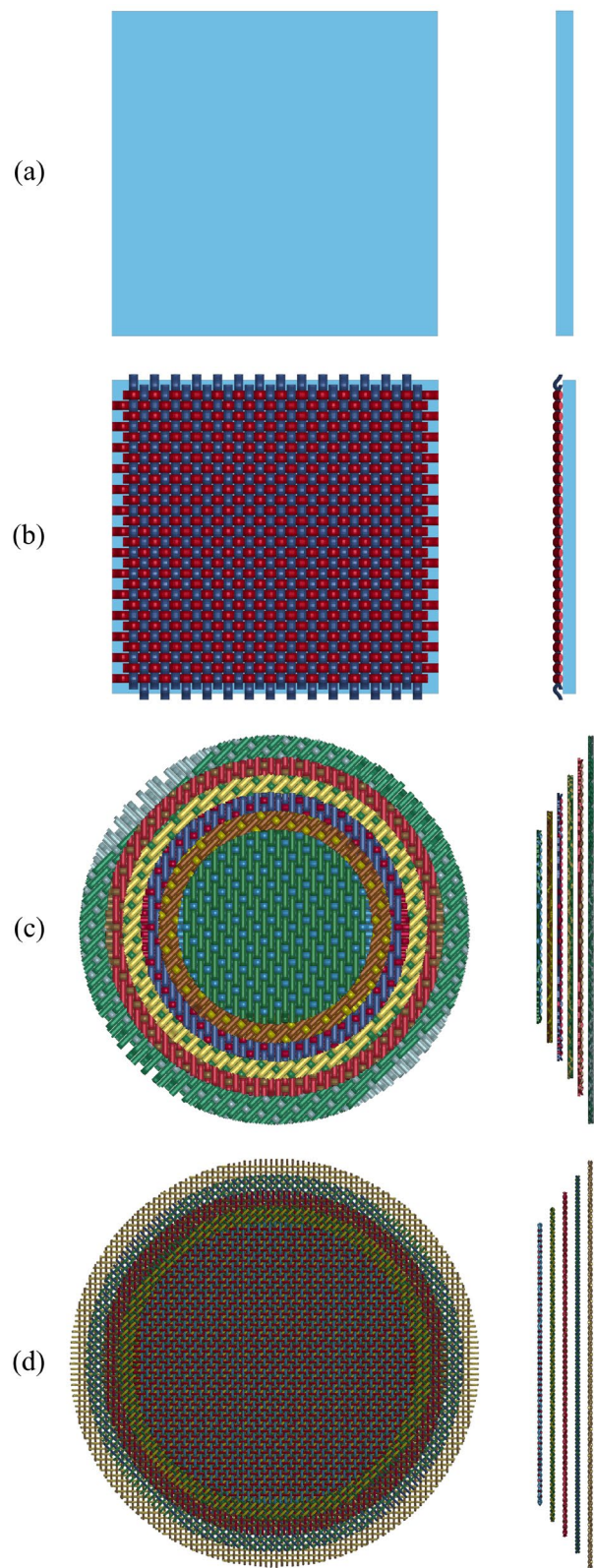


Figure 5: Numerical models of bumper configurations: (a) AA6061-T6, (b) Beta cloth + AA6061-T6, (c) Nextel AF-10, (d) SS 304 wire mesh.

3.2 Material models

3.2.1 Constitutive relations

The metallic materials in the study are modelled using a modified Johnson-Cook (MJC) constitutive relation [5][6], because of its simple calibration procedure and range of validity from low to high strain rates. It is a thermo-viscoplastic constitutive relation that accounts for strain hardening, strain-rate hardening and thermal softening. The equivalent stress σ_{eq} is given in Eqs. 1-3.

$$\sigma_{eq} = (\sigma_0 + R(p))(1 + \dot{p}^*)^C(1 - (T^*)^m) \quad (1)$$

and

$$R(p) = \sum_i Q_i(1 - e^{-C_i p}), \quad \dot{p}^* = \frac{\dot{p}}{\dot{p}_0} \quad (2)$$

$$T^* = \frac{T - T_0}{T_m - T_0}, \quad \Delta T = \int_0^p \chi \frac{\sigma_{eq} dp}{\rho C_p} \quad (3)$$

where σ_0 is the yield stress, Q_i and C_i are hardening parameters of an extended Voce hardening rule, p and \dot{p} are the equivalent plastic strain and strain rate, respectively, \dot{p}_0 is a user-defined reference strain rate, C governs the strain rate sensitivity of the material, T is the temperature, T_0 is a reference temperature, T_m is the melting temperature, and m governs the thermal softening of the material. Under the assumption of adiabatic conditions, which is reasonable in HVI, the temperature change ΔT is included, where χ is the Taylor-Quinney empirical coefficient, ρ is the material density, and c_p is the specific heat capacity. The material parameters for the MJC constitutive relation can be determined from uniaxial tension tests conducted at temperatures and strain rates suitable for the application at hand and are given for AA6061-T6, AA2017-T4 and SS 304 in Tab. 2.

The woven fabric materials in the study are modelled with a mesoscale approach, where the material model assumes homogeneous properties along the length of each yarn. The materials are assumed to be linearly elastic with orthotropic symmetry, with high stiffness along the length of each yarn, and low stiffness across the width and thickness of each yarn. Material parameters for Nextel and Beta cloth are presented in Tab. 3. The densities of the materials have been adjusted to match the areal density from the experiments.

3.2.2 Failure criteria

Failure of the metallic materials in the study can occur either when the element temperature reaches a critical temperature or when the Cockcroft-Latham (CL) failure criterion [15] is reached. The critical temperature T_c is set as 0.9 times the melting temperature T_m . The CL failure criterion is a phenomenological ductile fracture criterion depending on the plastic strain as well as the stress triaxiality ratio and the Lode angle through the maximum

principal stress σ_1 . The damage variable of the CL failure criterion is given by Eq. 4.

$$\omega = \frac{1}{W_c} \int_0^p \max(\sigma_1, 0) dp \quad (4)$$

The fracture parameter W_c is the only material constant, and is given for AA6061-T6, AA2017-T4 and SS 304 in Tab. 2.

The woven materials in the study are eroded and converted to discrete elements at a given failure strain. The failure strains for Nextel and Beta cloth are presented in Tab. 3.

Table 2: Parameters for the modified Johnson-Cook constitutive relation with Voce hardening, as well as general material parameters, for all the metallic materials in the study. For AA2017-T4 and SS 304, the Voce hardening parameters have been curve-fitted from JC power law hardening parameters, and the W_c parameters have been adjusted by trial and error.

Material	AA 6061-T6 [11]	AA 2017-T4 [16]	SS 304 [17]
Density, ρ [kg/m ³]	2700	2700	7800
Young's modulus, E [GPa]	70	70	210
Poisson's ratio, ν [-]	0.3	0.3	0.3
Yield stress, σ_0 [MPa]	292.6	270.0	325.2
Hardening parameter, Q_1 [MPa]	2.7	108.3	79.6
Hardening parameter, C_1 [-]	2160.7	114.6	26.3
Hardening parameter, Q_2 [MPa]	79.1	266.0	1194.5
Hardening parameter, C_2 [-]	8.94	3.47	1.21
Fracture parameter, W_c [MPa]	278	200	1000
Specific heat cap, C_p [J/kg·K]	9.1·10 ⁸	9.1·10 ⁸	5.1·10 ⁸
Taylor-Quinney coeff., χ [-]	0.9	0.9	0.9
Reference temperature, T_0 [K]	293	293	293
Melting temperature, T_m [K]	893	893	1600
Critical temperature, T_c [K]	804	804	1440
Strain rate parameter, C [-]	0.001	0.001	0.001
Softening parameter, m [-]	1	1	1
Thermal exp. coeff., α [K ⁻¹]	2.3·10 ⁻⁵	2.3·10 ⁻⁵	1.5·10 ⁻⁵

Table 3: Material parameters for the linearly orthotropic models for Nextel and Beta cloth.

Material	Nextel [18] [20]	Beta cloth [19]
Density, ρ [kg/m ³]	1320	2060
Young's modulus, longitudinal, E_l [GPa]	164	150
Young's modulus, transverse, E_t [GPa]	3.28	3.0
Poisson's ratio, ν [-]	0.15	0.125
Shear modulus, G [GPa]	1.64	24.2
Failure strain, p_f [-]	0.1	0.05

3.2.3 Equations of state

An equation of state (EOS) relates the pressure, volume, and internal energy of matter, and describes the hydrostatic behavior of the material. The non-linear Mie-Grüneisen EOS is commonly applied for numerical simulations of hypervelocity impact. However, studies [11] have found that the numerical results when using a linear EOS with the FEM/DEM method in LS-DYNA gave better results than the non-linear Mie-Grüneisen EOS for aluminum projectiles and shields. A linear EOS will therefore be applied in this study for all configurations and materials, to test its suitability for other configurations and materials. A linear EOS relates the pressure P to the volumetric strain ε_v linearly using the bulk modulus K , given in Eq. 5.

$$P(\varepsilon_v) = -K\varepsilon_v = -\frac{E}{3(1-2\nu)}\varepsilon_v \quad (5)$$

A linear EOS is therefore determined for a given material using only the two elastic material parameters.

4 NUMERICAL RESULTS

4.1 Debris clouds

The simulated debris clouds are presented in Fig. 7 around a similar time after impact for each bumper configuration. The results from the baseline and Beta cloth bumpers share similar characteristics, with a curved front, a concentration of projectile material at the front, followed by a half dome of particles, a high level of radial spread, and only a few elements from the projectile remaining in solid element form. Both are similar to the corresponding debris clouds from the experimental results. The debris cloud after impact with the Nextel bumper consists of a spherical concentration of projectile material, a lower level of radial spread and only a few elements remaining in solid element form. The outer shape is more oval than the experimental result but the amount of small dust particles in the experiment prohibits the comparison of the distribution of material inside the

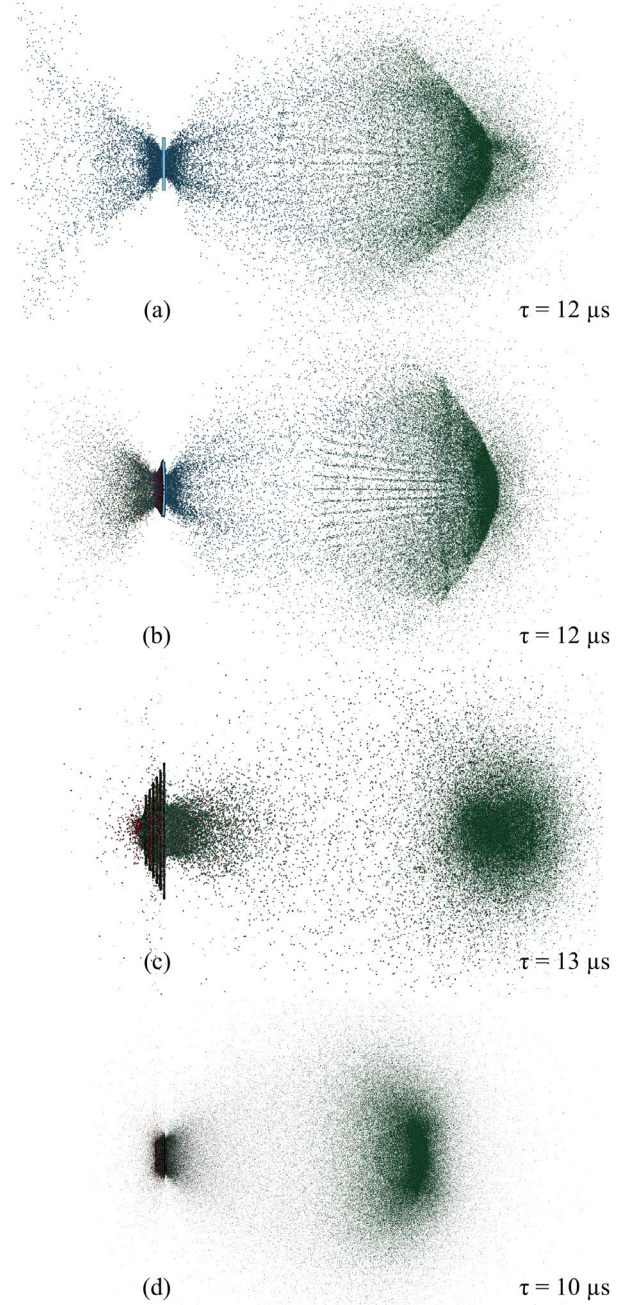


Figure 5: Debris clouds from simulations, around 10 μ s after impact for bumper configurations: (a) AA6061-T6, (b) Beta cloth + AA6061-T6, (c) Nextel AF-10, (d) SS 304 wire mesh.

debris clouds. The same is true for the debris cloud after impact with the SS 304 bumper. The simulation has a concentration of projectile material in a narrow disc at the front, followed by a small half dome of particles, a low level of radial spread, and a high number of elements still in solid form. Overall, the size and mass of the particles are different between the different configurations, stemming from larger elements in, e.g., the Nextel bumper, and very small elements in the SS 304 bumper.

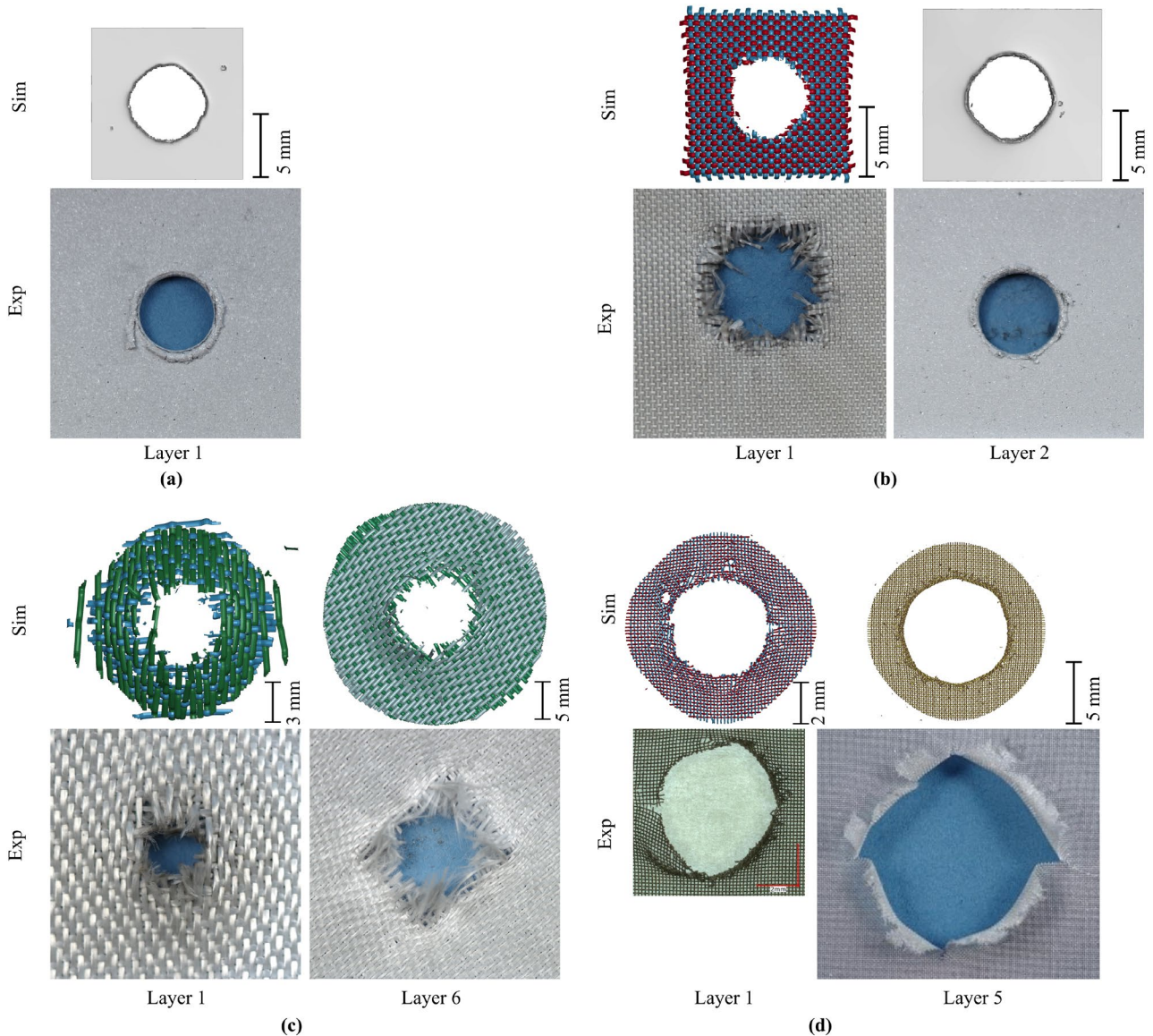


Figure 6: Comparison of the bumpers after impact from simulations (top) and experiments (bottom): (a) AA6061-T6, (b) Beta cloth + AA6061-T6, (c) Nextel AF-10, (d) SS 304 wire mesh.

The ejecta production is significantly different between the different simulations. Similar to the experiments, the baseline bumper generates the most ejecta with the highest velocity, followed by the Beta cloth bumper. The Nextel and SS 304 bumpers both produce very low amounts of ejecta in comparison, similar to the result from the experiments.

4.2 Bumper and rear wall damage

The front and rearmost layer in each bumper configuration after impact is presented in Fig. 8 for simulations and experiments. The hole in the baseline bumper is found to be of similar size and shape as in the experiment, around 5 mm. For the Beta cloth bumper, the holes in the AA6061-T6 layer and the Beta cloth layer are similar, both around 5 mm. The simulation matches the experiments on the inner hole measure of the Beta cloth,

but is unable to capture the fraying and unravelling of the individual fibers in the yarns. A similar result is found for the Nextel bumper. The hole diameter increases for each layer in both the simulation and experiment, and the inner measure of the hole diameter is similar. However, the fraying and unravelling is not fully captured by the homogeneous yarn model. The hole in the SS 304 bumper is also found to increase for each layer in the simulation, but the increase is less steep than in the experiments. The first layer is very similar to the experiment, with small holes and rips around a circular hole. The rearmost layer in the experiments show significant rips along the wire mesh directions, while the simulation gives a round, ordinary hole with a smaller diameter. Overall, the damage and hole diameters observed on the bumpers are found to be similar between the simulations and experiments.

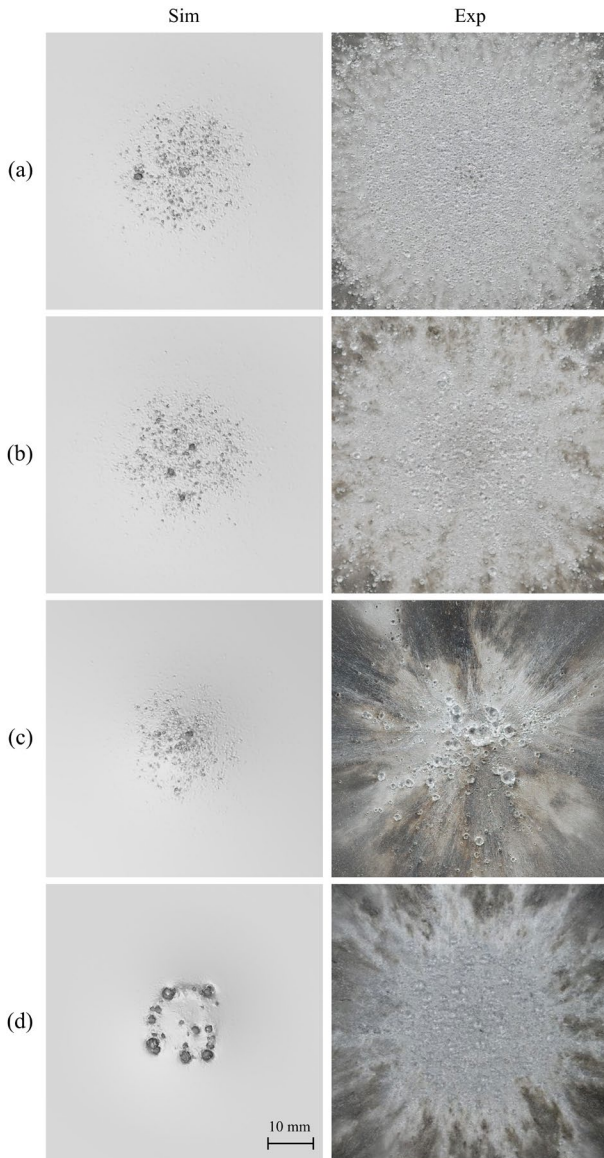


Figure 7: Comparison of rear walls after impact in simulations (left) and experiments (right) for bumper configurations: AA6061-T6, (b) Beta cloth + AA6061-T6, (c) Nextel AF-10, (d) SS 304 wire mesh.

The damage on the front side of the rear wall is presented in Fig. 9 for the experiments and simulations. The simulations of the baseline and Beta cloth bumper configurations both give circular concentrations of small craters in the center of the rear wall and a high level of radial spread. In the baseline configuration, a single medium-sized crater is found, while 3-4 are found for the Beta cloth configuration. The simulation of the Nextel bumper configuration is found to underestimate the crater size and depth compared to the experiments. A few medium-sized craters are observed, and all craters are located in a smaller area than for the baseline, but the high level of conversion to particles in the projectile prohibits the creation of larger and deeper craters on the

rear wall. The rear wall from the simulation of the SS 304 configuration is distinctly different than the others. A circle of larger craters are created around the center of the rear wall. The craters concentrated near the center of the rear wall in the experiments are slightly smaller than the ones seen in the simulations, and there are more of them inside a larger area.

Overall, the numerical models are able to capture with reasonable accuracy the debris clouds, ejecta production and damage to the bumpers, while some adjustments are recommended for the Nextel and SS 304 models to improve the craters on the rear wall.

5 CONCLUSIONS

An experimental and numerical study of hypervelocity impact on dual-wall Whipple shields is presented, focusing on the performance and behavior of different bumper materials impacted at 7 km/s. Three different material configurations (Beta cloth woven fabric with AA6061-T6, Nextel woven fabric, SS 304 metallic wire mesh) are compared to a traditional AA6061-T6 bumper, by dimensioning all bumpers to have near equal areal density around 0.17 g/cm^2 . Numerical models of the different configurations are created, and a coupled finite element-discrete element method (FEM-DEM) is applied to all materials, where failed elements are converted to particles. The simulations show an overall similarity to the experimental results, and create distinctly different debris clouds, ejecta characteristics, bumper hole diameters and crater patterns on the rear walls.

6 ACKNOWLEDGEMENTS

The authors wish to gratefully acknowledge the NASA JSC Hypervelocity Impact Technology (HVIT) group for supporting the test campaign, and the NASA White Sands Test Facility's Remote Hypervelocity Test Laboratory for performing the tests.

7 REFERENCES

- [1] F. L. Whipple, "Meteorites and Space Travel," *Astron. J.*, vol. 52, p. 131, 1947.
- [2] S. Ren *et al.*, "Review of bumper materials for spacecraft shield against orbital debris hypervelocity impact," *Def. Technol.*, 2024, doi: 10.1016/j.dt.2024.09.002.
- [3] H. Xu, J. Zhou, X. Cao, W. Liu, and C. Miao, "Energy absorption evaluation of multiple fabrics under hypervelocity impact loading," *Procedia Struct. Integr.*, vol. 52, no. 2022, pp. 52–62, 2024, doi: 10.1016/j.prostr.2023.12.006.
- [4] H. Xu, D. Yu, J. Cui, Z. Shi, D. Song, and C. Miao, "The Hypervelocity Impact Behavior and

- Energy Absorption Evaluation of Fabric,” *Polymers (Basel)*, vol. 15, no. 6, 2023, doi: 10.3390/polym15061547.
- [5] R. M. Færgestad *et al.*, “Hypervelocity impact on Whipple shields with varying bumper material at 3 and 7 km/s: An experimental study [accepted, in production],” *Int. J. Impact Eng.*, HVIS-2024 special issue, 2025.
- [6] N. N. Myagkov *et al.*, “Studies of the Fragmentation of Spherical Aluminum Projectiles on a Heavy Mesh at Velocities of up to 7 km/s,” *J. Exp. Theor. Phys.*, vol. 132, no. 2, pp. 177–188, 2021, doi: 10.1134/S1063776121020138.
- [7] N. N. Myagkov, T. A. Shumikhin, and L. N. Bezrukov, “Experimental and numerical study of peculiarities at high-velocity interaction between a projectile and discrete bumpers,” *Int. J. Impact Eng.*, vol. 37, no. 9, pp. 980–994, 2010, doi: 10.1016/j.ijimpeng.2010.04.001.
- [8] Livermore Software Technology (LST), “LS-DYNA, <https://www.lstc.com/products/ls-dyna> [accessed 30.05.2021].” 2021.
- [9] Dassault Systèmes, “Solidworks, <https://www.solidworks.com/> [accessed 15.02.2025].” 2025.
- [10] C. Geuzaine and J.-F. Remacle, “Gmsh, <https://gmsh.info/> [accessed 15.02.2025].”
- [11] R. M. Færgestad, J. K. Holmen, T. Berstad, T. Cardone, K. A. Ford, and T. Børvik, “Coupled finite element-discrete element method (FEM/DEM) for modelling hypervelocity impact,” *Acta Astronaut.*, vol. 203, pp. 296–307, 2023, doi: <https://doi.org/10.1016/j.actaastro.2022.11.026>.
- [12] Livermore Software Technology (LST), *LS-DYNA R12 Keyword User’s Manual*, vol. I. Livermore Software Technology Corporation (LSTC), 2020.
- [13] G. R. Johnson and W. H. Cook, “Fracture characteristics of three metals subjected to various strains, strain rates, temperatures and pressures,” *Eng. Fract. Mech.*, vol. 21, no. 1, pp. 31–48, 1985, doi: 10.1016/0013-7944(85)90052-9.
- [14] T. Børvik, O. S. Hopperstad, T. Berstad, and M. Langseth, “A computational model of viscoplasticity and ductile damage for impact and penetration,” *Eur. J. Mech. A/Solids*, vol. 20, no. 5, pp. 685–712, 2001, doi: 10.1016/S0997-7538(01)01157-3.
- [15] M. G. Cockroft and D. J. Latham, “Ductility and workability of metals,” *J. Inst. Met.*, vol. 96, pp. 33–39, 1968.
- [16] W. E. Bohl, J. E. Miller, E. L. Christiansen, and B. A. Davis, “HVI ballistic performance characterization of non-parallel walls,” in *Procedia Engineering*, 2013, vol. 58, pp. 21–30. doi: 10.1016/j.proeng.2013.05.005.
- [17] H. D. Espinosa, S. Lee, and N. Moldovan, “A Novel Fluid Structure Interaction Experiment to Investigate Deformation of A Novel Fluid Structure Interaction Experiment to Investigate Deformation of Structural Elements Subjected to Impulsive Loading,” *Exp. Mech.*, no. May 2014, 2006, doi: 10.1007/s11340-006-0296-7.
- [18] S. Hiermaier, W. Riedel, C.J. Hayhurst, R. A. Clegg, and C. M. Wentzel, “Advanced Material Models for Hypervelocity Impact Simulations,” 1999.
- [19] E. P. Fahrenthold, “Computational design of metal-fabric orbital debris shielding,” *J. Spacecr. Rockets*, vol. 54, no. 5, pp. 1060–1067, 2017, doi: 10.2514/1.A33736.
- [20] E. P. Fahrenthold, “Simulation of hypervelocity impact on aluminum-nextel-kevlar orbital debris shields,” *Int. J. Impact Eng.*, vol. 29, pp. 227–235, 2003.